Nonlinear Influence of T-Channels in an *in silico* Relay Neuron

Kai M. Hynna and Kwabena A. Boahen*, *Member, IEEE*

***Abstract*—Thalamic relay cells express distinctive response modes based on the state of a low-threshold calcium channel (T-channel). When the channel is fully active (*burst* mode), the cell responds to inputs with a high-frequency burst of spikes; with the channel inactive (*tonic* mode), the cell responds at a rate proportional to the input. Due to the T-channel's dynamics, we expect the cell's response to become more nonlinear as the channel becomes more active. To test this hypothesis, we study the response of an *in silico* relay cell to Poisson spike trains. We first validate our model cell by comparing its responses with *in vitro* responses. To characterize the model cell's nonlinearity, we calculate Poisson kernels, an approach akin to white noise analysis but using the randomness of Poisson input spikes instead of Gaussian white noise. We find that a relay cell with active T-channels requires at least a third-order system to achieve a characterization as good as a second-order system for a relay cell without T-channels.**

***Index Terms*—Neuroengineering, neuromorphic, relay cell model.**

I. Thalamic Relay Cells

THE THALAMUS is centrally located for much information ascending to the cortex. Excluding olfaction, all sensory input passes through one of its nuclei. For this reason, scientists often refer to the thalamus as the *gateway* to the cortex. Early thoughts on its role consisted of nothing more than a simple relay station for ascending information. Recent studies, however, suggest that the thalamus, with the massive feedback it receives from the cortex, may play an active role in information processing in the awake state [1].

Thalamic cells possess a low-threshold Ca^{++} channel, the activation of which dramatically alters the cell's output response. These channels—often called T-channels—are complicit in the generation of high-frequency bursts of action potentials, 2–6 spikes at frequencies greater than 250 Hz [20]. However, before the T-channel can cause a burst, it must first be deinactivated, accomplished through an extended period of hyperpolarization of the cell's membrane voltage—hundreds of milliseconds for full deinactivation [10].

When studying the influence of this channel, neuroscientists generally have considered its state in two extremes: fully deinactivated (*burst* mode) or fully inactivated (*tonic* mode). In these two modes, the response properties of the relay cell vary dramatically, not only in its firing patterns but also in properties such as temporal filtering [6], [21], [24], receptive field organization [7], [8], and representation of visual stimulus features [6], [19].

Our goal in this paper is twofold: First, we present our *in silico* model of a thalamic relay neuron—complete with a low-threshold calcium channel—and compare its behavior to real cells. Neuromorphic models are silicon reconstructions of neural circuitry, mimicking cellular-level ion-channel dynamics through similarities between transistors and ion channels [13]. Due to their compact designs, these models offer a means of studying the interaction among thousands of cells with biological realism, without slowing simulation speed.

Second, we characterize the model cell's nonlinearity in its two response modes using an approach similar to Wiener series analysis, except that instead of white noise current injections, we drive the cell with Poisson spike trains. We quantify the ability of the kernels thus obtained to capture the cell's behavior by using them to reproduce its output; the order of the kernels required to achieve a certain degree of fidelity serves as a measure of nonlinearity.

The kernel order is effectively the number of input spikes that interact to produce an output spike. For real relay cells, the efficacy of retinogeniculate synapses—defined as the percentage of input spikes generating an output spike—is approximately 30% [25]. Excluding other influences, such as proximity in time, this suggests that on average, three input spikes cause an output spike. Thus, we expect that a system order greater than one is necessary to capture the cell's behavior in tonic mode. We expect the system order to be even higher in burst mode, given the T-channel's complex dynamics.

We begin by providing a background on Poisson series, briefly comparing it to its predecessor the Wiener series, and describing its underlying mathematics (Section II). In the next section, we continue by describing our relay cell model and verifying its operation (Section III). Following that, we proceed with the analysis, first by describing our approach, and then presenting our computed kernels (Section IV). We then quantify these kernels' ability to capture the model's nonlinear behavior by using them to recreate its output (Section V). The paper concludes with a discussion (Section VI).

II. Poisson Series

The Poisson approach is an extension of the Wiener series, using the statistics of Poisson input spikes—rather than white

Manuscript received April 26, 2008; revised October 21, 2008 and December 23, 2008. First published March 4, 2009; current version published June 10, 2009. This work was supported in part by the Packard Foundation and in part by the National Science Foundation's CAREER Program under Grant ECS00-93851. *Asterisk indicates corresponding author.*

K. M. Hynna was with the Department of Bioengineering, University of Pennsylvania, Philadelphia, PA 19104 USA. He is now with Ethoca Technologies, Toronto, ON, Canada (e-mail: kai.hynna@gmail.com).

*K. A. Boahen was with the University of Pennsylvania, Philadelphia, PA 19104 USA. He is now with the Department of Bioengineering, Stanford University, Stanford, CA 94305 USA (e-mail: boahen@stanford.edu).

Digital Object Identifier 10.1109/TBME.2009.2015579

noise—to calculate the system kernels. Wiener series analysis [18], [23]—also called white noise analysis—has been applied extensively over the past few decades to many sensory systems, especially visual (for a brief review, see [23]). The advantage of a technique like this, in addition to being simple (procedurally) to perform, is that it bypasses many of the details of the transduction process (e.g., of light to current for vision), and results in a set of kernels that are intuitive—at least in the first-order case—to the researcher. In addition, the extension of the single-input model to multiple inputs allows the vision researcher to expand the white noise stimulus spatially to study spatiotemporal behavior—the *receptive field* of the cell. This approach has been used successfully to study temporal contrast adaptation in both salamander ganglion [14] and bipolar cells [22], to study contrast sensitivities in ON and OFF ganglion cell pathways [27] as well as to study Na^{+} inactivation in the salamander retinal ganglion cell [15].

For central neural systems, away from sensory periphery, Wiener series analysis can still be used—through white noise current injection—to study a cell's internal, postsynaptic dynamics. However, for these neurons, using trains of action potentials is potentially more informative [17]. Using input spikes to probe the response of a cell lumps synaptic processing with membrane filtering and provides a spike-in to spike-out system description. Neurons do not operate their ion channels in isolation of their synapses, and so the Wiener series, while useful for understanding isolated membrane components, may be less valuable in understanding a neural system's function. Poisson kernels were first used to study synaptic transmission in lobsters [16], [17].

A system's response to a Poisson spike train is represented by

$$\begin{aligned} y(t) = \mathrm{g}_0 &+ \int_{-\infty}^{\infty} \mathrm{g}_1(\sigma)\ x(t-\sigma)\ \mathrm{d}\sigma \\ &+ \int_{-\infty}^{\infty}\int_{-\infty}^{\infty}_{\sigma_1\neq\sigma_2} \mathrm{g}_2(\sigma_1,\sigma_2)\, x(t-\sigma_1) \\ &\times\ x(t-\sigma_2)\ \mathrm{d}\sigma_1\ \mathrm{d}\sigma_2 + \cdots \end{aligned} \tag{1}$$

where g_n is the nth-order kernel and $x(t) = \sum_i \delta(t - t_i)$ is the input Poisson spike train with rate λ, with each spike represented by a Dirac delta function ($\delta(t)$). Note the restriction on the diagonal of the integration variables ($\sigma_1 \neq \sigma_2$) for the second (and higher) order integrals. This restriction removes additional terms that occur at $\sigma_1 = \sigma_2$ when calculating the kernels (described next). In the Wiener series, these additional terms are removed using lower order kernels [18]. The same approach is not possible with Poisson spike trains, due to differences in the input statistics, and thus the need for the restriction on the integral [17].

Before calculating the kernels g_n, we must first calculate an intermediate set of kernels for the following system:

$$\begin{aligned} y(t) = \mathrm{z}_0 &+ \int_{-\infty}^{\infty} \mathrm{z}_1(\sigma)\ x_p(t-\sigma)\ \mathrm{d}\sigma \\ &+ \int_{-\infty}^{\infty}\int_{-\infty}^{\infty}_{\sigma_1\neq\sigma_2} \mathrm{z}_2(\sigma_1,\sigma_2)\, x_p(t-\sigma_1) \\ &\times\ x_p(t-\sigma_2)\ \mathrm{d}\sigma_1\ \mathrm{d}\sigma_2 + \cdots \end{aligned} \tag{2}$$

where $x_p(t) = x(t) - \lambda$ is the zero-mean Poisson spike train—the spike train equivalent of Gaussian white noise in the Wiener series. Like the system expression for Wiener series, each integral expression in (2) is a functional, and to help isolate the kernels' forms, these functionals are constrained to be orthogonal to each other. Thus, to calculate the kernels z_n, the expectation of the output and an appropriate number of inputs isolates each functional [17]

$$\begin{aligned} \mathrm{z}_0 &= \mathrm{E}[y(t)] \\ \mathrm{z}_1(\sigma) &= \frac{1}{\lambda}\mathrm{E}[y(t)\,x(t-\sigma)] - \mathrm{z}_0 \\ \mathrm{z}_2(\sigma_1,\sigma_2) &= \frac{1}{2}\left(\frac{1}{\lambda^2}\mathrm{E}[y(t)\,x(t-\sigma_1)\,x(t-\sigma_2)]\right. \\ &\qquad \left. - \mathrm{z}_1(\sigma_1) - \mathrm{z}_1(\sigma_2) - \mathrm{z}_0\right) \end{aligned}$$

where $E[\cdot]$ is the expectation over the stimulus period [17]. Since $x(t)$ consists of Dirac delta functions, calculating the expectation simply becomes a sum of the output function sampled at different intervals by the input. For example, in the first-order kernel calculation, the expectation is

$$\begin{aligned} \mathrm{E}[y(t)\,x(t-\sigma)] &= \int_0^T y(t)\ x(t-\sigma)\ dt \\ &= \int_0^T y(t)\ \sum_i \delta(t - t_i - \sigma)\ dt \\ &= \sum_i y(t_i + \sigma). \end{aligned}$$

The relationship between the kernels z_n and g_n are calculated by substituting $x_p(t) = x(t) - \lambda$ into (2) and grouping terms of the same integral order together. The variable g_i is then the sum of functionals z_j, where $i \leq j \leq n$ (with n being the order of the system). For example, for a third-order system

$$\begin{aligned} \mathrm{g}_0 = \mathrm{z}_0 &- \lambda\int_{-\infty}^{\infty} \mathrm{z}_1\ \mathrm{d}\sigma_1 + \lambda^2 \int_{-\infty}^{\infty}\int_{-\infty}^{\infty}_{\sigma_1\neq\sigma_2} \mathrm{z}_2\ \mathrm{d}\sigma_1\mathrm{d}\sigma_2 \\ &- \lambda^3 \int_{-\infty}^{\infty}\int_{-\infty}^{\infty}\int_{-\infty}^{\infty}_{\sigma_1\neq\sigma_2\neq\sigma_3} \mathrm{z}_3\ \mathrm{d}\sigma_1\,\mathrm{d}\sigma_2\,\mathrm{d}\sigma_3 \end{aligned}$$

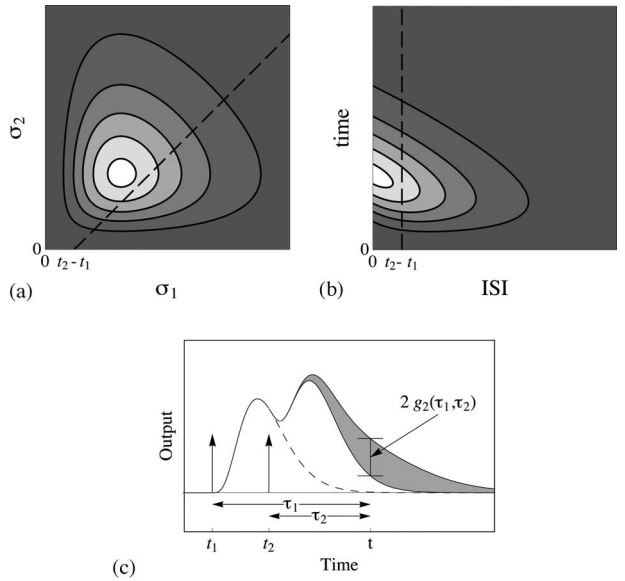

Fig. 1. Second-order kernel. (a) Contour plot showing a sample second-order kernel (arbitrary output units). Background gray represents zero and increasing lighter shades representing increasing positive values. The ISI $\sigma_2 - \sigma_1$ between pairs of input spikes defines the second-order effect (dashed line). (b) Kernel from (a) drawn with a change of variable. Time from second spike is isolated to one axis, with ISI on the other. (c) Sample output response to two input spikes (vertical arrows). In a linear system, the output would be the sum of individual linear kernels (black solid line, shaded white). The ISI defines the second-order effects, and manifests itself on top of the linear response (shaded gray).

$$\mathrm{g}_1(\sigma_1) = \mathrm{z}_1 - 2\lambda \int_{-\infty}^{\infty} \mathrm{z}_2 \, \mathrm{d}\sigma_2 + 3\lambda^2 \int_{-\infty}^{\infty} \int_{-\infty}^{\infty} \mathrm{z}_3 \, \mathrm{d}\sigma_2 \mathrm{d}\sigma_3$$
$$\sigma_2 \neq \sigma_3$$

$$\mathrm{g}_2(\sigma_1, \sigma_2) = \mathrm{z}_2 - 3\lambda \int_{-\infty}^{\infty} \mathrm{z}_3 \, \mathrm{d}\sigma_3$$

$$\mathrm{g}_3(\sigma_1, \sigma_2, \sigma_3) = \mathrm{z}_3.$$

For each additional order included in the system, the lower order kernels are modified by removing some of the higher order influences. The difference between a second- and third-order system is simply all of the aforementioned terms containing z_3. The mean output of the system, however, remains constant regardless of the system order.

Kernel interpretation for a spike train stimulus, given its discrete nature, is much more intuitive than for Gaussian white noise. The linear kernel g_1 is the response of the system to each individual input spike. The second-order kernel g_2, which is more difficult to understand in the continuous input case, demonstrates the response of the cell to two spikes *on top of* the sum of the individual linear kernels (Fig. 1). Extending to higher orders, the nth-order kernel represents the effect on the output of the system from combinations of n spikes. For ease of presentation, we will rearrange the second-order and higher order kernels so that they show the response of the system to the *interspike interval* (ISI) of input spikes [compare Fig. 1(a) with Fig. 1(b)].

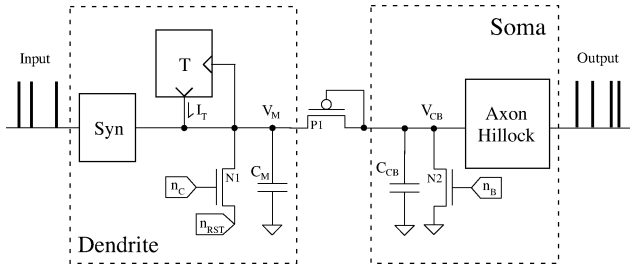

Fig. 2. Relay cell model. The *in silico* cell consists of two compartments: a dendrite, which receives input spikes and contains the T-channel circuit, and a soma, which generates output spikes. See text for details.

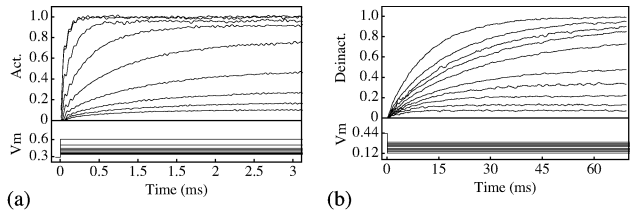

Fig. 3. T-channel gating dynamics *in silico*. (a) I_{T} activation in response to step changes of the membrane voltage V_{M} (bottom). V_{M} begins low so that the activation variable is zero, and steps to higher voltages. The activation level increases with V_{M}, approaching steady state more slowly at intermediate levels of V_{M}. (b) I_{T} deinactivation in response to step changes of the membrane voltage V_{M} (bottom). V_{M} begins high so that I_{T} is inactivated, and steps to lower voltages. The deinactivation level increases with decreasing V_{M}; as in activation, the dynamics are slower at intermediate levels of V_{M}.

III. Silicon Relay Cell

Our silicon relay cell consists of two compartments (Fig. 2): a dendritic compartment to integrate inputs and a somatic one to generate outputs. The dendritic compartment contains all active membrane components not involved in spike generation—namely, the T-channel and synaptic circuits—as well as common passive membrane components—a membrane capacitance (C_{m}) and a membrane conductance (transistor N1).

The synapse circuit [2] is based on a simple kinetic synapse model that represents biophysical mechanisms of transmitter release and binding to receptors [5]. It converts spikes into synaptic currents, tuned such that we achieve a 5-ms time-constant matching those observed in excitatory alpha-amino-3-hydroxy-5-methyl-4-isoxazolepropionic acid (AMPA) receptors [4], [9]. The efficacy of the synapse is set to roughly 30%, as seen at the retinogeniculate synapse [25], using a 10-Hz input Poisson spike train (in simulated real time; see discussion of *hypertime* later). We transmit spikes to and from our chip over a digital link using *address events* [3].

The T-channel circuit has been described in detail previously [12]. Briefly, it uses two channel variables to model the activation and inactivation dynamics of the low-threshold calcium channel. The activation variable [13] takes advantage of thermodynamic similarities between transistor channels and ion channels to capture the voltage dependence of both the steady state and time constant of the variable. The inactivation variable [12] is based upon similar principles, but we use a different approach to achieve the slower inactivation dynamics found in real cells. Activation opens the channel as V_{M} increases [Fig. 3(a)], initiating a burst; inactivation, which operates much slower, closes

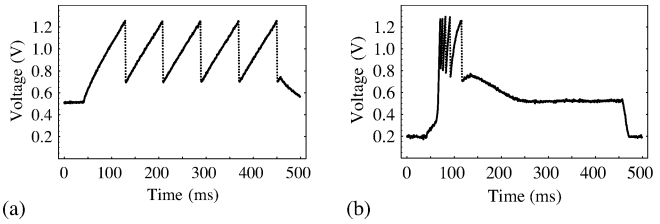

Fig. 4. Dendritic voltage ($V_{\rm M}$) records for the cell's two firing modes. (a) Tonic. (b) Burst. In tonic mode, $V_{\rm M}$ is initially high ($\approx$500 mV), which inactivates $I_{\rm T}$. In burst mode, $V_{\rm M}$ is initially low ($\approx$200 mV), which deactivates $I_{\rm T}$. For both figures, a 400-ms-wide current step is injected into the dendritic compartment at $t = 50$ ms. The soma's spike does not propagate back to the dendrite due to the axial diode between the two compartments. Instead, the dendritic compartment only reflects the reset component of the cell body's spike.

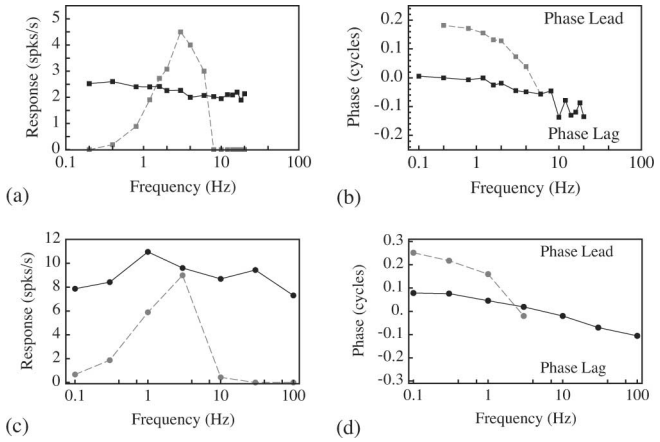

Fig. 5. Frequency responses in the two firing modes: burst (dashed, gray) and tonic (solid, black). (a) Mean response and (b) phase are extracted from a Fourier transform of the peristimulus time histogram (PSTH), each trial corresponding to the spikes recorded in a single cycle [24]. The cell's response mode is adjusted through the mean current level of the input sinusoid. [(c) and (d)] Mean response and phase from a real relay cell (data replotted from [24]).

the channel, ending the burst. $V_{\rm M}$ needs to lower sufficiently to deactivate the channel before another burst can occur [Fig. 3(b)]. The product of these two variables defines the T-channel current ($I_{\rm T}$), which we feed directly into the dendritic compartment.

The somatic compartment integrates current received from the dendritic compartment on its capacitor ($C_{\rm CB}$) and generates spikes. The main component within this compartment models the axon hillock, which causes the cell to generate a spike once a voltage threshold is surpassed. The axon hillock circuit also activates interface circuitry that transmits the spike of-chip as an address event.

Connecting the two compartments is a diode-connected transistor (transistor P1). Due to its rectifying behavior, this diode allows current to pass only from the dendrite to the soma. As a result, the somatic action potential does not propagate back to the dendrite (Fig. 4); only the hyperpolarization (reset) that follows is evident in the dendritic voltage trace ($V_{\rm M}$). This is a simple approximation of dendritic low-pass filtering of the back-propagating signal.

The dendritic voltage spans a range of 0–1.2 V. This corresponds to a cellular voltage range of approximately -120 to -45 mV, the latter being the spike threshold of the cell. The mapping is not perfectly linear, given our membrane conductance's nonlinear dynamics; in addition, the activation and inactivation thresholds of the T-channel are slightly lower relative to the spike threshold than seen *in vivo*. This would appear as a slight temporal shift in the position of the burst, as $I_{\rm T}$, once activated, needs to raise $V_{\rm M}$ further. While this should be taken into consideration when interpreting our results, qualitatively we do not feel they will change.

Our silicon circuits' temporal dynamics are faster than seen in biology, i.e., our chips run in *hypertime*, for reasons discussed in [11]. This feature allows us to collect large amounts of data in a practical amount of time. However, when presenting our results, we have scaled our data in time by a *hypertime factor*, such that the time scale of our measured results—which we call *simulated real time*—matches biological time scales. More specifically, we scaled time such that the time constant of our T-channels are similar to those seen within relay neurons, to facilitate comparing *in silico* and *in vitro* results.

The results in this paper are measured from two different chips, both fabricated in 0.25 μm CMOS. Due to differences in transistor dimensions, however, these chips possess different hypertime factors. For the results presented in this section, the hypertime factor is 5 (i.e., our chip ran five times faster than biology). For the results presented in Section IV, the hypertime factor is 10. For instance, the 10-Hz input that we used to set our synaptic weight is defined in *simulated real time*; in real time (i.e., not scaled by our hypertime factor), our input spike train had a mean rate of 100 Hz.

A. Current Clamp Response

We use a current clamp experiment to demonstrate our cell's different modes (Fig. 4). If we initialize the dendritic resting potential at depolarized levels—$V_{\rm M} \approx 500$ mV, sufficiently high to inactivate the T-channel—the cell responds to a step input current with a constant-rate spike train [Fig. 4(a)]. Immediately after the step ($\approx$50 ms), $V_{\rm M}$ begins to rise, and current eventually passes into the somatic compartment via the axial diode. $V_{\rm M}$ continues to increase linearly until $V_{\rm CB}$ reaches spike threshold, the point at which the axon hillock generates a spike. After spike reset, dendritic integration continues. Since $V_{\rm M}$'s trajectory is linear, the firing rate increases linearly with input current (data not shown), as observed in real relay cells [20].

Next, we repeat the procedure with a constant inhibitory current added to the injected current step [Fig. 4(b)]. The inhibitory current lowers the initial $V_{\rm M}$ to approximately 200 mV, thereby deactivating $I_{\rm T}$. After the step, $V_{\rm M}$ begins to rise; at around 400 mV, $I_{\rm T}$ activates, causing a rapid rise in $V_{\rm M}$ and initiating a burst. The initial spike rate approaches 200 Hz, decreasing with each successive spike as the channel inactivates, and eventually the cell stops firing.

B. Frequency Response

Another measure that we can use to validate our *in silico* model is its frequency response (Fig. 5). Real thalamic cells change their response from bandpass in burst mode to all-pass in tonic mode [Fig. 5(c)]. Our cell shows a similar change from

burst to tonic [Fig. 5(a)]. In burst mode, spiking is entirely due to I_{T}, as the maximum input current is insufficient to cause the cell to spike. At high frequencies (above 3 Hz), the cell spends less time at low membrane voltages, and I_{T} does not have sufficient time to deactivate, and spike rates start to drop, eventually ceasing. At medium frequencies (from 0.5 to 3 Hz), I_{T} has enough time to fully deactivate, and the cell fires a burst with the same number of spikes every cycle; thus, the response is proportional to stimulus frequency. At low frequencies (below 0.5 Hz), I_{T} begins to inactivate before it can activate, and the number of spikes per burst decreases. Thus, there is a sublinear increase in spike rate with stimulus frequency.

In tonic mode, the T-channel is always inactive, and so the response is dependent solely on the input current, which the cell simply integrates. At low frequencies, the cell responds with multiple spikes on top of the sinusoid peak. As the frequency increases, the number of spikes within each cycle decreases. At frequencies greater than the mean spike rate, the cell no longer is capable of generating spikes at every cycle, but responds subharmonically. This results in a flat frequency response, as the number of spikes per cycle is inversely proportional to the stimulus frequency.

The response's phase also matches to that seen in *in vitro* [Fig. 5(b) and (d)]. In burst mode, the response leads at low frequencies; the T-channel activates and induces a burst before the input peak. This lead disappears as the frequency increases, and eventually, the response lags. The latency is due to the channel's activation dynamics and membrane integration. For low frequencies, the latency is negligible compared to the stimulus period, and so, as the frequency drops, the phase asymptotes to the position where the input current overcomes the membrane leak. As the frequency increases, the latency becomes more significant, delaying the burst toward the input's peak, and eventually, past it.

In tonic mode, the response always lags [Fig. 5(b)], due to temporal integration by the membrane capacitance. Only at low frequencies, where this latency becomes negligible with respect to the stimulus period, with spikes distributed approximately equally before and after the input peaks, does the tonic phase approach zero. As the period shortens, the latency becomes significant, causing a greater phase lag. *In vitro* measurements show a similar shift toward a phase lag. Real cells, however, begin with a phase lead that becomes a phase lag as the frequency increases [Fig. 5(d)]. The discrepancy is due to frequency adaptation within real neurons, which results in a stronger initial response—and thus a phase lead—at low frequencies.

Even though our *in silico* data match *in vitro* data well qualitatively, there are quantitative differences between them: the absolute spike rates are higher *in vitro*, the peak response for burst mode is higher than tonic mode *in silico*, and the burst phase *in silico* falls off at higher frequencies than *in vitro*. However, our focus is to characterize the T-channel dynamics and not the cell as a whole, which possesses numerous other currents that our model does not include.

IV. Poisson Kernels

To study nonlinearity, we will calculate the Poisson kernels for our *in silico* neuron. We represent our system by two serial operations (Fig. 6): a temporal filter that processes incoming input spikes and a current-to-frequency converter that generates output spikes. These operations correspond to the two compartments within our model cell (Fig. 2).

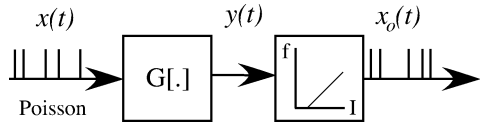

Fig. 6. System diagram of a neuron. $\mathrm{G}[\,.\,]$ performs temporal filtering, representing the action of synaptic and membrane dynamics on the input spike train ($x\,(t)$). This operator's output $y\,(t)$ is converted to a spike train ($x_o\,(t)$) by a second operator, representing integration of current supplied by the dendrite to a fixed threshold at the axon hillock.

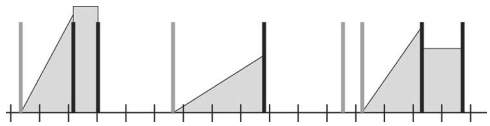

Fig. 7. Converting the output spike train to a rate function. Each qualified ISI is replaced by a function whose integral (gray) over the ISI is unity. A qualified ISI is defined as one between an output spike and the closest spike preceding it, either output (black) or input (gray). In the former case, the function has zero slope; in the latter case, it has non-zero slope and starts from zero—a simple representation of synapse dynamics.

Our interest lies in characterizing the operator $\mathrm{G}[\,.\,]$, which we can represent using (1). Before computing the kernels, however, we must first obtain the *output rate function* ($y\,(t)$) from the measured output spike train ($x_o\,(t)$). To do so, we must invert the second operation (i.e., the action of the axon hillock). In its simplest form, it integrates the input and generates a spike once a fixed threshold is reached. After each spike, the integral resets to zero and integration resumes. And as such, the output spike rate is proportional to $y\,(t)$, averaged over a time interval immediately preceding the output spike. When considering *instantaneous spike rate*, the time interval is the ISI between output spikes. We, however, define the start of this time interval as the closer (to the output spike) of either the previous output spike or the preceding input spike.

For intervals defined by consecutive output spikes, we place a unit-area pulse with height inversely proportional to the ISI (Fig. 7). For intervals defined by an input–output spike pair, we place a ramp that increases linearly from zero—the firing rate before the input arrived—to a height such that its integral is unity. This ramp is a simplified representation of synaptic interactions: the input arrives at the synapse and generates an output that increases from zero.

We ignore input–output pairs shorter than a fixed minimum interval—defined as the smallest *output* ISI within the complete tonic data set. This choice prevents any part of the output rate function from becoming abnormally large. This is reasonable because an input spike cannot trigger an output spike infinitely fast—the minimum latency is set by the postsynaptic current's peak amplitude and rise time. Once we have obtained the output rate function, we can compute our kernels.

In either firing mode (tonic or burst), we drive the cell with identical 10 Hz Poisson spike trains and record the output spike trains. At this input rate, the mean ISI is 100 ms, which is

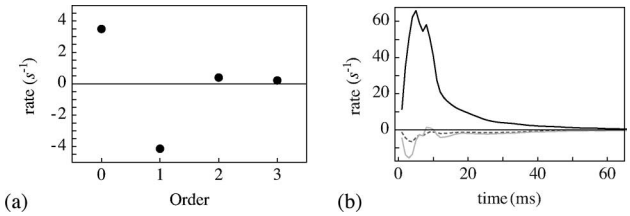

Fig. 8. Zeroth- and first-order kernels for tonic mode (10 Hz input). (a) Variable g_0 for zeroth-, first-, second-, and third-order systems. As the order of the system increases, g_0's magnitude decreases, suggesting there is no constant output, but rather the response is stimulus-dependent. (b) Variable g_1 for first-order (black, solid), second-order (gray, solid), and third-order (dashed) systems. In the higher order systems, g_1 virtually disappears.

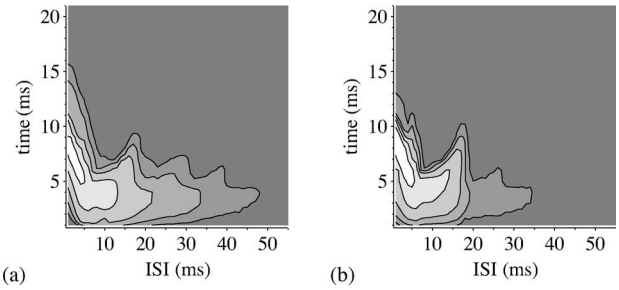

Fig. 9. Second-order kernels for tonic mode. (a) Second-order system. (b) Third-order system. Unlike the second-order system, the third-order system's g_2 does not include interactions at long ISIs (ISI $>$ 20 ms). Contour lines are drawn at 15, 30, 60, 125, and 250 spikes/s. For this and all contour plots, 0 spikes/s falls within the background gray area; negative rates are darker while positive rates are lighter. The contours in each plot vary, and are chosen to highlight differences between kernels.

sufficient time for I_{T} to deactivate more often than not in burst mode.

Using both input and output spike trains, we obtain the output rate function and calculate kernels for systems of order zero to three. For our kernels, we use 200 bins with a binwidth of 1 ms, for a kernel width of 200 ms, sufficiently long to capture all the interactions for both modes.

A. Tonic Mode

In tonic mode, only synaptic and membrane dynamics are present, since we set the resting potential of the cell sufficiently high to inactivate I_{T}. In describing the kernels in this (and the following) sections, we will proceed by kernel order (e.g., describing all the first-order kernels for systems of various orders), rather than by system order (e.g., describing all the kernels for a first-order system). This choice facilitates comparisons between the system representations.

All four systems (order zero through three) possess g_0 [Fig. 8(a)]. For the zeroth-order system, g_0 is 3.5 spikes/s, the neuron's mean output rate. For the first-order system, g_0 is negative, offsetting the first-order kernel's contribution to the output rate to match the mean output rate. For second- and third-order systems, g_0 becomes positive again, but approaches zero with higher orders. This is an encouraging indication that, for our 10 Hz input, our higher order systems are successfully capturing system dynamics.

The variable g_1 for a first-order model [Fig. 8(b)] demonstrates a form similar to synaptic dynamics: a sudden rise to a peak, followed by a decay to zero. When we increase the system order from two or three, g_1 essentially disappears, indicating that the response is described better by the higher order kernels. This is not surprising considering we chose the synaptic weights to necessitate multiple input spikes for output activity. However, a residual contribution—the initial negative bump—remains; this could be an artifact created by crosstalk between digital and analog circuits.

The variable g_2 for both a second- and third-order system have similar forms (Fig. 9). Two input spikes less than 10 ms apart generate a tall peak, whose height (321.8 and 373.9 spikes/s for second- and third-order systems, respectively) indicates the occurrence of two output spikes with a short ($<$3.5 ms for both systems) interval. As the input ISI increases, the peak disappears; the system now responds with a lower spike rate—a single spike—that declines with increasing ISI. This decline, however, is more pronounced in the third-order system; its response disappears for ISIs greater than 20 ms. Apparently, these longer ISI interactions are better captured by the third-order kernel, indicating that they are the result of interactions among more than two spikes. This effect suggests that temporal integration occurs only for synaptic inputs that are less than 20 ms apart.

Only the third-order system has a third-order kernel. The variable g_3 is a 3-D structure, which we can rearrange such that two-dimensions represent the two successive ISIs within a spike triplet, and the third-dimension represents the response's evolution in time from the third spike. We plot snapshots of g_3 taken at different intervals between the second and third spikes (Fig. 10). When this interval $\mathrm{ISI}_1 = 1$ ms, we see two prominent zones of interaction: One occurring 5–10 ms after the triplet for $\mathrm{ISI}_2 < 10$ ms, and another occurring immediately after the triplet for $\mathrm{ISI}_2 > 10$ ms.

The first interaction zone has a negative trough that corresponds in time with the peak in g_2 [Fig. 9(b)], and a positive peak that appears immediately afterward. The effect of the trough would be to suppress the triplet's g_2 contributions (from pairwise combinations of its spikes). The effect of the peak would be to compensate for the resulting drop in mean rate by producing an uptick, albeit a little latter in time. These effects suggest that spike-triplet responses are more spread out in time than one would expect from spike-doublet responses, and likely reflects saturation in the synaptic current. This first interaction zone disappears when ISI_2 increases to 10 ms, which corresponds to when g_2's peak disappears.

The second interaction zone consists of a (smaller) positive peak, which extends out to longer ISI_1 times. The effect of this peak is to produce an uptick in output rate immediately ($<$5 ms) after the triplet—unlike the first zone's peak, which produces a delayed response ($>$5 ms). This effect suggest that, even though synaptic activity has decayed too much for spike pairs to cause an output spike (g_2 effectively disappears at 20 ms), there is sufficient residual activity for triplets to do so. Conversely, the disappearance of g_3 when either interval is around 10 ms suggests

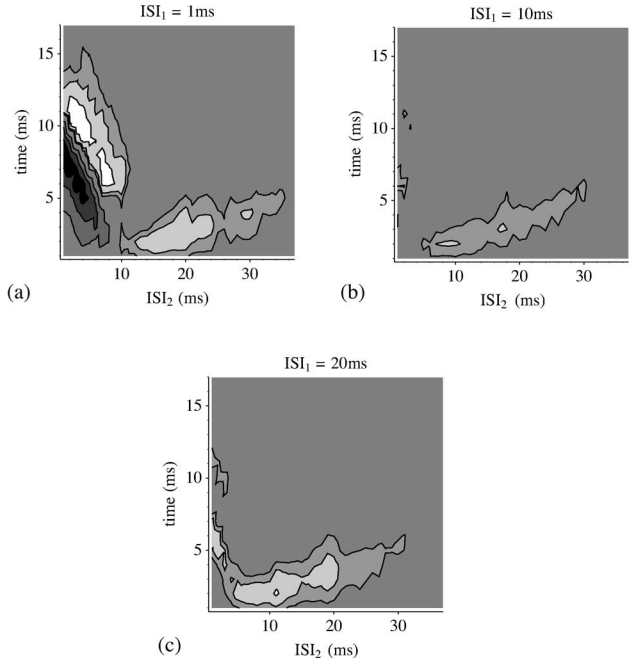

Fig. 10. Third-order kernels for tonic mode. Snapshots at different intervals (ISI_1) between the second and third spikes of a triplet are shown; ISI_2 is the interval between the first and second spikes. (a) Variable g_3 at $\mathrm{ISI}_1 = 1$ ms, (b) $\mathrm{ISI}_1 = 10$ ms, and (c) $\mathrm{ISI}_1 = 20$ ms. Two zones of interactions are evident: The first is most pronounced when ISI_1 is extremely short; the second is most pronounced when both ISI_1 and ISI_2 are about 20 ms. Contour lines are drawn at $-150, -100, -50, 15, 30$, and 60 spikes/s.

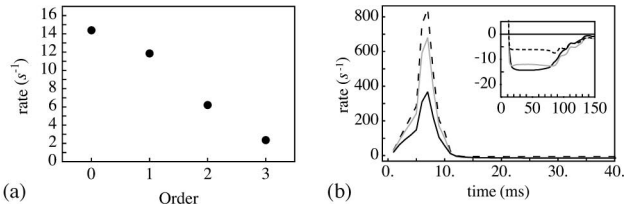

Fig. 11. Zeroth- and first-order kernels in burst mode (10 Hz input). (a) Zero-order kernels for zeroth-, first-, second-, and third-order systems. As the order of the system increases, g_0 decreases, reflecting the fact that the higher order kernels account for more and more of the output spikes. (b) g_1 for first-order (solid, black), second-order (solid, gray), and third-order (dashed) systems. The positive peak is followed by a negative trough (inset).

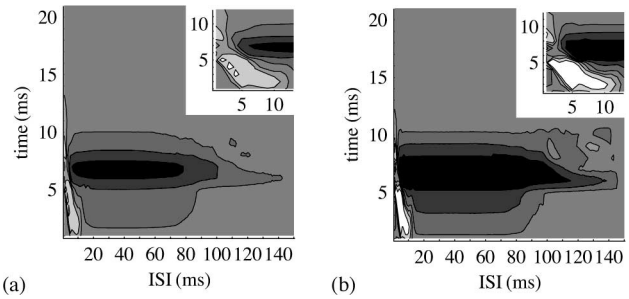

Fig. 12. Second-order kernels for burst mode. (a) Second-order system. (b) Third-order system. Both kernels display a trough that extends to long ISIs and a peak at short ISIs. The inset expands the kernels at the low ISIs. Contour lines are drawn at $-150, -75, -25, 25, 75$, and 150 spikes/s.

that the third spike is superfluous in this case; just two suffice to produce an output spike.

B. Burst Mode

The kernels change dramatically when we lower the resting potential of the dendritic voltage to switch the cell from tonic mode to burst mode. Looking at the zeroth-order system's g_0 [Fig. 11(a)], we see that the cell's mean output rate is higher than in tonic mode (14.4 versus 3.5 Hz). This increase reflects the action of I_{T}, which, due to our choice of a 10 Hz input rate, is deinactivated more often than when a spike arrives. Due to I_{T}'s low threshold for activation, this spike can trigger a burst all by itself—whereas multiple spikes are required to produce just one spike in tonic mode. This arrangement explains the increase in mean output rate. As the system order increases, we see a decrease in g_0 (as in the tonic case), indicating an improved ability to capture the neuron's dynamics.

When we look at g_1, we see that it has a much taller and tighter peak than the tonic system, and a negative trough that was not present before [Fig. 11(b)]. The larger peak represents output bursts; the negative trough represents inactivation—its length corresponds to the time I_{T} needs to deactivate. In the first-order system, the trough is not deep enough to prevent another burst—it only marginally reduces the burst peak (by less than 5%)—it represents inactivation by countering g_0 after a burst.

Unlike the tonic case, g_1 does not disappear in the second- and third-order systems; rather, its peak is enhanced. This enhancement suggests that, even though a single spike can trigger a burst, there are many instances when this does not occur. Indeed, we expect this to be the case when this spike follows the previous one too closely, providing insufficient time for I_{T} to deiactivate. These pairwise (and multispike) interactions are captured by the higher order kernels, making g_1 a truer reflection of what happens in the case of a single isolated spike when the system order increases. Thus, the enhanced peak is a more accurate reflection of the burst's influence.

When we look at g_2, we see a long trough that extends out to $\mathrm{ISI} = 100$ ms for both second- and third-order systems (Fig. 12). This trough's position in time matches g_1's peak, suggesting the following interaction between it, and g_2:g_1 captures the response to each input spike, which is by default a burst; g_2 modulates the size of the burst by capturing the previous spike's contribution to channel inactivation. This interaction explains the increase in g_1's peak with increasing system order—g_2's trough is deeper in the third-order system, roughly accounting for the difference in peak height.

The variable g_2 has a second salient feature: a peak at small ISIs, which likely represents synaptic influences. Since a single spike can trigger a burst, the synaptic response around the burst (from 5 to 10 ms) is also captured by g_1. The remainder of its synaptic response (0–5 ms) stays in g_2. This explains why the peak in g_2 in burst mode occurs earlier than in tonic mode, where all the synaptic response appeared in g_2.

When we look at g_3 (Fig. 13), we get a glimpse of how the higher order kernels help in modulating g_1's response, which now more accurately represents the structure of a canonical burst (i.e., one invoked by an isolated spike). The modulation is

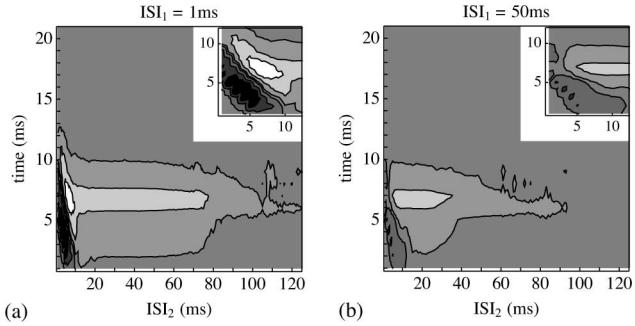

Fig. 13. Third-order kernels for burst mode. Snapshots at different intervals between the second and third spikes of a triplet (ISI_1) are shown; ISI_2 is the interval between the first and second spike. (a) $\mathrm{ISI}_1 = 1$ ms. (b) $\mathrm{ISI}_1 = 50$ ms. The trough and peak—which correspond in time to g_2's peak and trough, respectively [Fig. 12(b)]—are most pronouced when the second and third spikes occur in close succession. Contour lines are drawn at -80, -45, -10, 10, 45, and 80 spikes/s.

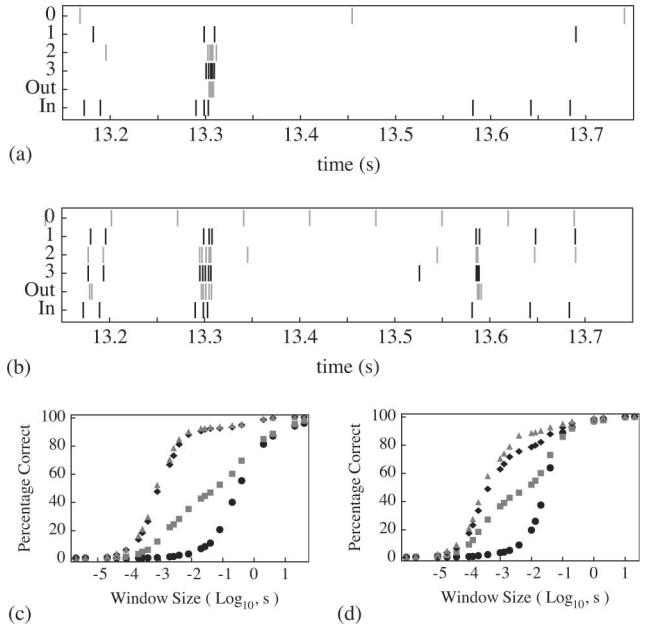

Fig. 14. [(a) and (c)] Performance of Poisson kernels in tonic mode and [(b) and (d)] burst mode. [(a) and (b)] Spike trains for stimulus (in), actual response (out), and predicted response (0,1,2, and 3 for respective system order). Note that the stimulus is the same in both cases. [(c) and (d)] Percentage of spikes predicted correctly versus window size. Zeroth-, first-, second-, and third-order systems (black circles, gray squares, black diamonds, and gray triangles, respectively) are plotted.

strongest when the triplet's last two spikes occur close together [Fig. 13(a)]. When they occur less than 10 ms after the triplet's first spike, there is a positive contribution from five separate kernel instantiations: two pairings—between the first spike and both of the other two—output the peak from g_2, and each individual spike contributes g_1. The trough in g_3 is positioned to suppress these contributions, suggesting a nonlinear interaction within the triplet. The fact that this trough—and the subsequent peak—becomes less pronounced as the second-to-third spike interval increases [Fig. 13(b)], recapping g_3's behavior in tonic mode, suggests saturation plays a role in burst mode as well.

When the triplet's second and third spike occur more than 10 ms after its first spike, we see a positive bump that extends up to 80 ms—it shortens as the second-to-third spike interval lengthens [Fig. 13(b)]. This bump coincides with g_2's trough, whose length [100 ms in Fig. 12(b)] matches the length of triplets that fall in the bump (the longest first-to-last spike interval in Fig. 13's snapshots are $78 + 1$ and $35 + 50$ ms). Thus, the g_1 burst from the third spike is suppressed by two g_2 troughs, caused by first and third, and second and third spike pairs. However, only a single trough is necessary to suppress the burst from the third spike, and thus, this second trough is superfluous and would prolong inactivation too much. Thus, g_3's bump reduces the magnitude of this double trough.

V. Kernel Evaluation

We evaluate the Poisson kernels by using them to predict the cell's output. Convolving the kernels with an input spike train (1) produces a time-varying rate. This rate is input to an integrator (see Fig. 6) to produce an output spike train. A spike is generated once the integral reaches a fixed threshold, which we set to unity, corresponding to the unit-area shapes used to obtain the (instantaneous) rate from the actual spike train (see Fig. 7).

Unsurprisingly, prediction accuracy improves as system order increases [Fig. 14(a) and (b)]. Starting with uniformly distributed spikes in the zeroth-order case, spikes move to their correct locations with increasing order; the mean output rate remains constant. However, even for the third-order system, spurious spikes did occur (e.g., at $t = 13.55$ s in burst mode), because g_0 is still nonzero. We calculate the percentage of spikes predicted correctly to quantify performance. This measure is adequate since, regardless of system order, the output rate is constant. We paired predicted spikes with actual spikes using an algorithm designed to calculate a distance metric for spike trains [26]. This algorithm matches individual spikes between two spike trains (in our case, the real and predicted spikes) by minimizing a cost function. For each matched pair, a cost is incurred equal to the time interval between the spikes multiplied by an interval cost parameter. The algorithm also adds (or deletes) spikes from either train at a fixed cost; thus, paired spikes will fall within a fixed time window, defined as the fixed cost of adding/deleting a spike divided by the interval cost. This interval cost—or its inverse, the window size, which we use—is the free parameter within the metric.

In both burst and tonic modes, the percentage of spikes predicted correctly improved with increasing system order [Fig. 14(c) and (d)]. In tonic mode, the percentage increases dramatically from first- to second-order, but hardly at all from second to third. For 2 ms precision, the percentage jumps from 28% to 81% to 85% for first-, second-, and third-order systems, respectively. For 4 ms, it jumps from 36% to 88% to 91%. This suggests that a second-order system suffices to capture the cell's behavior in tonic mode. In burst mode, while the improvement from first- to second-order is still the most dramatic, the improvement from second- to third-order is significant. For 2 ms, the percentage jumps from 43% to 72% to 79% for first-,

second-, and third-order systems, respectively. For 4 ms, the percentage jumps from 46% to 76% to 87%.

Comparing performance in the two modes, zeroth- and first-order systems perform better in burst mode than they do in tonic mode, whereas the reverse is true in for second- and third-order systems. Zeroth-order does better in burst mode simply because the spike rate is higher—its just luck. First-order does better in burst mode because just one spike is required to trigger a burst—it gets the timing right. Whereas second- and third-order do better in tonic mode for the nontrivial reason that the cell's dynamics are simpler: the only thing you have to predict is the spike's timing. In burst mode, in addition to timing, you also have to predict the number of spikes within each burst, which is much more dependent on the presence of previous inputs. Both second- and third-order burst systems do well with timing, but the latter does better at predicting the number of spikes in a burst [Fig. 14(b)]. Third-order's 7%–9% performance edge also comes from its ability to eliminate spurious spikes (g_0 drops from 6.2 to 2.3 spikes/s). In terms of absolute performance, third-order does about as good a job in burst mode as second-order does in tonic mode (79% versus 81% and 87% versus 88% for 2–4 ms precision, respectively).

VI. Discussion

We studied an *in silico* relay neuron consisting of electronic circuits representing the T-channel, the cell, and a single excitatory synapse. Our goal was to characterize I_T's role in the cell's behavior using Poisson kernels, which isolate interactions of different orders by exploiting the statistical properties of Poisson spike trains. They are similar to Wiener kernels, which use white noise as input (either as current injections or sensory stimuli). Driving the cell with Poisson spikes rather than white noise has two distinct advantages: First, synaptic dynamics are included, whereas when current is injected directly into the cell, they are ignored. Second, Poisson kernels provide an intuitive description: the nth-order kernel describes how n spikes interact to contribute to the output. A more detailed comparison between the two approaches can be found in [17].

We evaluated the ability of Poisson kernels to capture the cell's behavior by using them to predict its spike train. A second-order system performed as well in tonic mode as a third-order system did in burst mode (81% versus 79%, respectively, for 2 ms precision), confirming our hypothesis that behavior was more nonlinear in burst mode. Increasing the system order from two to three yielded negligible improvement in tonic mode, suggesting that pairwise spike interactions sufficed to capture most of the cell's synaptic and membrane dynamics. As we were careful to calibrate the model's synaptic and membrane properties with physiological measurements (e.g., matching synaptic strength and time course), we expect the second-order system's performance to hold up *in vivo*.

A third-order system yielded significant improvement over a second-order system in burst mode (from 72% to 79% for 2 ms precision). This improvement stems from the third-order system's greater ability to generate a more canonical burst and to suppress responses to input spikes that arrive within the inactivation period after a burst. With the *in silico* cell's resting potential set such that I_T deactivates, the default response is a burst, which shows up as a tall peak in the first-order kernel. Since any response is I_T-dependent, the arrival of an input spike after a burst will cause a response dependent on the level of I_T deinactivation. The troughs in g_2 [Fig. 12(a)] enact this response modulation. The deeper troughs in g_2 of the third-order burst system [Fig. 12(b)], however, are much better at eliminating the postburst response (data not shown). The third-order kernels (Fig. 13) then work to counter the deep troughs from g_2 in situations where there are more than two spikes.

When using Poisson kernels to study a system, it is important to consider a couple of (related) points. First, since the approach is rate constant, using a system order that is too small for the system's interactions will result in the lower order kernels accounting for the higher order (nonrepresented) interactions; the higher order kernels effectively "pollute" the lower order kernels. We saw this pollution with decreasing system order, most prominently within g_1 in tonic mode when increasing the system order from 1 [Fig. 8(b)], but also in burst mode in the increase of the burst peak in g_1 with increasing system order [Fig. 11(b)]. When looking at the highest order kernel, it may not be immediately clear which aspects of it are from—or being suppressed by—even higher order interactions.

Second, the presence of higher order dynamics are strongly dependent on the Poisson spike train statistics (i.e., the input frequency), which means the system order necessary to achieve a sufficient performance level also relies on these statistics. For example, had we used an extremely low input spike frequency—say 0.1 Hz—the probability of a second spike arriving within the deinactivation period of the T-channel would be very low. In this scenario, a first-order system would perform very well, since I_T would likely be fully deinactivated when each input spike arrives. In our case, we knew the temporal dynamics of the underlying interactions ahead of time, and therefore, chose an appropriate input frequency. Without prior knowledge, varying the frequency and observing the changes in the kernels would be necessary to obtain information on the system's temporal dynamics. The first-order kernel of a first-order system will not change with input frequency if the underlying system consists only of first-order interactions, but will change if higher order interactions exist.

These caveats are relevant in interpreting our results. Looking at the tonic system's g_2, it is clear that most of the relevant input spike interactions occur when the second spike arrives within 20 ms of the first. The T-channel, by contrast, extends spike interactions out to 100 ms, and, as a result, higher order kernels are necessary to accurately represent the burst system. However, had we used a higher input frequency, more spikes may have fallen within the tonic system interaction window, and a second-order system would be insufficient to represent the tonic mode. This does not contradict our conclusion that the burst mode is more nonlinear, since at this higher frequency, a burst system would require an even greater system order to capture its operation. So the relevant point here is that I_T extends the interactions at the input to longer times than simply the synapses alone, and thus will always be more nonlinear.

One of the benefits of this approach is its flexibility: it is not limited to studying ion channels, but can be used to study other cell processes that involve spikes as inputs. This includes interactions at the synapse (e.g., depression), and the influence of other neurotransmitters (e.g., γ-aminobutyric acid (GABAergic) inputs). In addition, while our simple model used only a single input spike train, the model can easily be expanded to include multiple input pathways. With independent Poisson spike trains at each input, cross kernels can be calculated for the interactions between the separate pathways, in addition to kernels for each individual pathway.

Future work involves expanding our *in silico* relay cell studies in these directions. In this paper, we used the cell's resting potential to set it's mode: higher voltages for tonic mode and lower ones for burst mode. As a result, a burst was dependent on the absence of excitatory input to allow for T-channel deinactivation. *In vivo* cells in awake mammals, however, generally rest in tonic mode, and so any T-channel response relies on inhibitory mechanisms to deactivate I_{T}. Adding an inhibitory synapse to our *in silico* cell would allow us to study the interactions of the excitatory and inhibitory input spikes and their influence on the cell's behavior.

ACKNOWLEDGMENT

The authors would like to thank G. Smith for providing frequency response data measured from real cells.

REFERENCES

[1] H. J. Alitto and W. M. Usrey, "Corticothalamic feedback and sensory processing," *Current Opinion Neurobiol.*, vol. 13, no. 4, pp. 440–445, 2003.

[2] J. V. Arthur and K. A. Boahen, "Synchrony in silicon: The gamma rhythm," *IEEE Trans. Neural Netw.*, vol. 18, no. 6, pp. 1815–1825, Nov. 2007.

[3] K. A. Boahen, "Point-to-point connectivity between neuromorphic chips using address events," *IEEE Trans. Circuits Syst. II, Analog Digit. Signal Process.*, vol. 47, no. 5, pp. 416–434, May 2000.

[4] A. Destexhe, T. Bal, D. A. McCormick, and T. J. Sejnowski, "Ionic mechanisms underlying synchronized oscillations and propagating waves in a model of ferret thalamic slices," *J. Neurophysiol.*, vol. 76, no. 3, pp. 2049–2070, 1996.

[5] A. Destexhe, Z. F. Mainen, and T. J. Sejnowski, "Synthesis of models for excitable membranes, synaptic transmission and neuromodulation using a common kinetic formalism," *J. Comput. Neurosci.*, vol. 1, no. 3, pp. 195–230, 1994.

[6] M. S. Grubb and I. D. Thompson, "Visual response properties of burst and tonic firing in the mouse dorsal lateral geniculate nucleus," *J. Neurophysiol.*, vol. 93, no. 6, pp. 3224–3247, 2005.

[7] W. Guido, S. M. Lu, and S. M. Sherman, "Relative contributions of burst and tonic responses to the receptive field properties of lateral geniculate neurons in the cat," *J. Neurophysiol.*, vol. 68, no. 6, pp. 2199–2211, 1992.

[8] W. Guido and T. Weyand, "Burst responses in thalamic relay cells of the awake behaving cat," *J. Neurophysiol.*, vol. 74, no. 4, pp. 1782–1786, 1995.

[9] S. Hestrin, "Different glutamate receptor channels mediate fast excitatory synaptic currents in inhibitory and excitatory cortical neurons," *Neuron*, vol. 11, no. 6, pp. 1083–1091, 1993.

[10] J. R. Huguenard and D. A. McCormick, "Simulation of the currents involved in rhythmic oscillations in thalamic relay neurons," *J. Neurophysiol.*, vol. 68, no. 4, pp. 1373–83, 1992.

[11] K. M. Hynna, "T channel dynamics in a silicon LGN," Ph.D. dissertation, Univ. Pennsylvania, Philadelphia, 2005.

[12] K. M. Hynna and K. Boahen, "Silicon neurons that burst when primed," in *Proc. IEEE Int. Symp. Circuits Syst. (ISCAS 2007)*, pp. 3363–3366.

[13] K. M. Hynna and K. Boahen, "Thermodynamically-equivalent silicon models of ion channels," *Neural Comput.*, vol. 19, pp. 327–350, 2007.

[14] K. J. Kim and F. Rieke, "Temporal contrast adaptation in the input and output signals of salamander retinal ganglion cells," *J. Neurosci.*, vol. 21, no. 1, pp. 287–299, 2001.

[15] K. J. Kim and F. Rieke, "Slow Na+ inactivation and variance adaptation in salamander retinal ganglion cells," *J. Neurosci.*, vol. 23, no. 4, pp. 1506–1516, 2003.

[16] H. I. Krausz and W. O. Friesen, "The analysis of nonlinear synaptic transmission," *J. Gen. Physiol.*, vol. 70, no. 2, pp. 243–265, 1977.

[17] H. I. Krausz, "Identification of nonlinear systems using random impulse train inputs," *Biol. Cybern.*, vol. 19, no. 4, pp. 217–230, 1975.

[18] Y. W. Lee and M. Schetzen, "Measurement of the kernels of a nonlinear system by cross-correlation," *Int. J. Control*, vol. 2, pp. 237–254, 1965.

[19] N. A. Lesica and G. B. Stanley, "Encoding of natural scene movies by tonic and burst spikes in the lateral geniculate nucleus," *J. Neurosci.*, vol. 24, no. 47, pp. 10731–10740, 2004.

[20] D. A. McCormick and H. R. Feeser, "Functional implications of burst firing and single spike activity in lateral geniculate relay neurons," *Neuroscience*, vol. 39, no. 1, pp. 103–113, 1990.

[21] P. Mukherjee and E. Kaplan, "Dynamics of neurons in the cat lateral geniculate nucleus: In vivo electrophysiology and computational modeling," *J. Neurophysiol.*, vol. 74, no. 3, pp. 1222–1243, 1995.

[22] F. Rieke, "Temporal contrast adaptation in salamander bipolar cells," *J. Neurosci.*, vol. 21, no. 23, pp. 9445–9454, 2001.

[23] H. M. Sakai, "White-noise analysis in neurophysiology," *Physiol. Rev.*, vol. 72, no. 2, pp. 491–505, 1992.

[24] G. D. Smith, C. L. Cox, S. M. Sherman, and J. Rinzel, "Fourier analysis of sinusoidally driven thalamocortical relay neurons and a minimal integrate-and-fire-or-burst model," *J. Neurophysiol.*, vol. 83, no. 1, pp. 588–610, 2000.

[25] W. M. Usrey, J. B. Reppas, and R. C. Reid, "Specificity and strength of retinogeniculate connections," *J. Neurophysiol.*, vol. 82, no. 6, pp. 3527–3240, 1999.

[26] J. D. Victor and K. P. Purpura, "Metric-space analysis of spike trains: Theory, algorithms and application," *Netw.: Comput. Neural Syst.*, vol. 8, no. 2, pp. 127–164, 1997.

[27] K. A. Zaghloul, K. Boahen, and J. B. Demb, "Different circuits for on and off retinal ganglion cells cause different contrast sensitivities," *J. Neurosci.*, vol. 23, no. 7, pp. 2645–2654, 2003.

Kai M. Hynna received a B.A.Sc. degree in systems engineering from the University of Waterloo, Waterloo, ON, Canada, in 1998, and the Ph.D. degree from the Department of Bioengineering, University of Pennsylvania, Philadelphia, in 2005, where he was engaged in understanding neural processing in thalamic cells using neuromorphic models of ion channels.

He is currently with a private company in Toronto, ON, Canada.

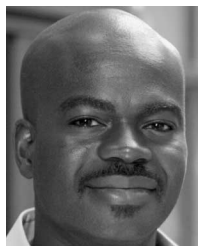

Kwabena A. Boahen (M'99) received the B.S. and M.S.E. degrees in electrical and computer engineering from Johns Hopkins University, Baltimore, MD, in 1989, and the Ph.D. degree in computation and neural systems from California Institute of Technology, Pasadena, in 1997.

He received the Sloan Fellowship for Theoretical Neurobiology from California Institute of Technology. From 1997 to 2005, he was a Faculty Member at the University of Pennsylvania, Philadelphia, where he was also the first Skirkanich Term Junior Chair. He is currently an Associate Professor in the Department of Bioengineering, Stanford University, Stanford, CA. He is a Bioengineer who uses silicon-integrated circuits to emulate the way neurons compute, linking the seemingly disparate fields of electronics and computer science with neurobiology and medicine. His contributions to the field of neuromorphic engineering include a silicon retina that could be used to give the blind sight and a self-organizing chip that emulates the way the developing brain wires itself up. His scholarship is widely recognized, with over sixty publications to his name, including a cover story in the May 2005 issue of Scientific American.

Dr. Boahen had received several distinguished honors, including a Fellowship from the Packard Foundation in 1999, the CAREER Award from the National Science Foundation in 2001, the Young Investigator Award from the Office of Naval Research in 2002, and the National Institutes of Health DirectorÕs Pioneer Award in 2006. He is a member of Tau Beta Kappa.